



A Gaussian reflective metasurface for advanced wavefront manipulation

Downloaded from: <https://research.chalmers.se>, 2026-04-03 14:59 UTC

Citation for the original published paper (version of record):

Martinez Llinas, J., Clément, H., André, D. et al (2019). A Gaussian reflective metasurface for advanced wavefront manipulation. *Optics Express*, 27(15): 21069-21082.

<http://dx.doi.org/10.1364/OE.27.021069>

N.B. When citing this work, cite the original published paper.



A Gaussian reflective metasurface for advanced wavefront manipulation

JADE MARTÍNEZ-LLINÀS,¹ CLÉMENT HENRY,^{1,2} DANIEL ANDRÉN,¹
RUGGERO VERRE,¹ MIKAEL KÄLL,^{1,3} AND PHILIPPE TASSIN¹

¹*Department of Physics, Chalmers University of Technology, SE-412 96 Göteborg, Sweden*

²*Department of Electronics and Telecommunications, Politecnico di Torino, IT-10129 Turin, Italy*

³*mikael.kall@chalmers.se*

Abstract: Metasurfaces enable us to control the fundamental properties of light with unprecedented flexibility. However, most metasurfaces realized to date aim at modifying plane waves. While the manipulation of nonplanar wavefronts is encountered in a diverse number of applications, their control using metasurfaces is still in its infancy. Here we design a metareflector able to reflect a diverging Gaussian beam back onto itself with efficiency over 90% and focusing at an arbitrary distance. We outline a clear route towards the design of complex metareflectors that can find applications as diverse as optical tweezing, lasing, and quantum optics.

© 2019 Optical Society of America under the terms of the [OSA Open Access Publishing Agreement](#)

1. Introduction

Metasurfaces are artificially engineered arrays of subwavelength-spaced optical scatterers patterned on a flat surface [1–6]. The basic concept was introduced long ago in millimeter and microwave technology to manipulate the wavefronts of light by spatially patterning an interface [7–11]. Through advances in nanofabrication, this concept has nowadays been extended to visible light, as nanopatterning tools allow us to induce local and abrupt phase changes to light at the subwavelength scale. The wavefronts of reflected and transmitted beams can be engineered nearly at will by adjusting material and geometrical parameters such as size, shape, separation, and orientation of the metasurface building blocks.

The subwavelength separation of the metamaterial building blocks not only enables the control of the phase, amplitude, and polarization of light at high spatial resolution, but also avoids the formation of spurious diffraction orders, which appear in conventional diffractive optical systems such as gratings. In the past few years, metasurfaces have been used for applications such as cloaking [12–15], absorbing and antireflection coatings [16–18], high-resolution imaging [19,20], focusing [21–24], slow light [25], polarization control [26–28], energy harvesting [29], and tunable beam steering [30]. The versatility in their design together with their straightforward fabrication, which usually involves a single-step lithographic process, makes metasurfaces good candidates to realize multifunctional flat photonic devices [3,31,32].

Despite large efforts, metasurfaces are most often designed to manipulate plane waves [33–35]. This is mainly because a plane wave is independent of the position of illumination on the metasurface, which significantly simplifies the computational complexity during the design stage as it allows for the use of periodic boundary conditions. Light beams with more complex wavefronts do not have this translation symmetry, and therefore require the simulation of full device structures of the order of tens of micrometers. This often leads to design problems that are computationally too expensive even for modern powerful computers. Nevertheless, the possibility of modifying beams with strongly shaped wavefronts rather than plane waves is of very high importance, in particular for reflectors, i.e., optical elements able to reflect a light beam back to its source with minimal scattering. Such reflectors would be interesting for creating confocal cavities in vertical-cavity semiconductor lasers or for optical tweezers.

In this article, we show that it is indeed possible to simulate and design metasurfaces that can

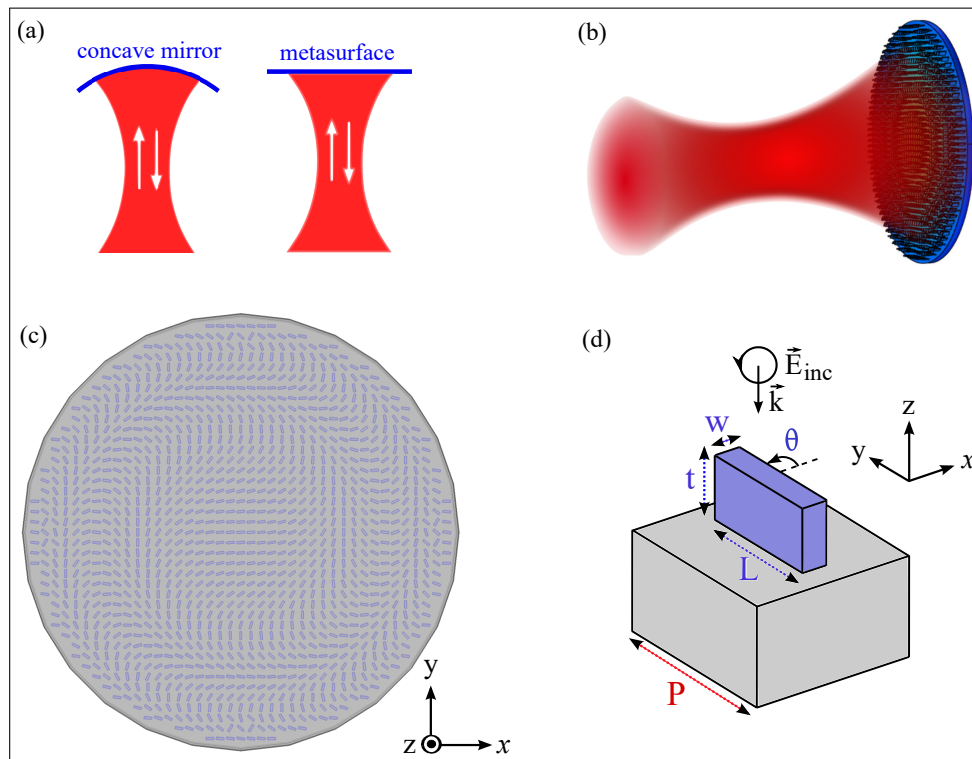


Fig. 1. Concept and design of the reflective metasurface: (a) Spherical concave mirror (left) and metasurface with the same behavior as a concave mirror (right) reflecting an incoming beam. (b) Gaussian reflective metasurface reflecting a Gaussian beam back onto itself. (c) Top view of the metasurface designed to reflect a circularly polarized Gaussian beam. All the nanofins have the same dimensions and their angle of rotation changes with the square of their distance from the center. (d) Unit cell consisting of a nanofin on top of a substrate. The efficiency of the metasurface can be optimized by adjusting the height (t), length (L), and width (w) of the nanofins and the unit cell size (P). The 2π phase coverage can be obtained by varying the angle of rotation (θ).

reflect light beams with strongly shaped wavefronts by combining numerical computation and far-field propagation methods. Specifically, we design a metasurface that can reflect a Gaussian beam at visible and near-infrared wavelengths with high efficiency [see Fig. 1(a)-1(b)]. This system is the metasurface equivalent of a concave spherical mirror. We realize such a metasurface using dielectric nanofins [see Fig. 1(c)-1(d)] that act as half-wave plates in reflection. By properly choosing the orientation of the nanofins and taking into account the coupling between elements with full-wave numerical simulations of the whole structure, we design a mirror that is able to refocus a Gaussian beam to the same focal point as the incident beam.

2. Metasurface design

The design of the reflective metasurface is divided into three steps. First, we determine the phase profile of the mirror required to reshape a given incoming beam. Second, we optimize the values of the geometrical parameters of the building blocks of the metasurface in order to maximize the efficiency of the mirror. Finally, we construct the entire mirror by mapping the required phase profile with meta-atoms of appropriate orientations.

2.1. Phase profile of the mirror

To determine the required phase profile, we consider the reflection of a Gaussian beam from a concave spherical mirror. Among the many possible beam shapes a reflector can manipulate, Gaussian beams are indeed the most relevant because of their simple cylindrical symmetry and their experimental relevance. We choose the mirror to be located at $z = 0$ and the incoming beam propagating in the $-z$ direction. For Gaussian beams, the electric field is of the form [36]:

$$E(\rho, \phi, z) = E_0(z) \exp\left(-\frac{\rho^2}{w^2(z)}\right) \exp\left(-i\frac{k\rho^2}{2\mathcal{R}(z)}\right) \exp(i\psi(z)), \quad (1)$$

where (ρ, ϕ, z) are cylindrical coordinates, k is the wave number, $\mathcal{R}(z)$ is the radius of curvature of the phase fronts, and $w(z)$ is the spot size. The phase fronts are determined by the imaginary exponential factors, of which the arguments can be rewritten in the form

$$\Phi_{\text{inc}}(\rho, \phi, z) = A(z)k\rho^2 + \Phi_{\text{inc}}(\rho = 0, \phi, z), \quad (2)$$

where we have isolated the phase contribution that depends on ρ , because it is this contribution that controls the curvature of the phase fronts (the other contribution is just a constant phase shift at the plane of the mirror). For Gaussian beams, $A(z) = 1/(2\mathcal{R}(z))$, where

$$\mathcal{R}(z) = z \left[1 + \left(\frac{z_0}{z}\right)^2 \right] \quad (3)$$

is the radius of curvature of the phase fronts and z_0 is the Rayleigh distance. In the paraxial approximation, the complex reflection amplitude of a spherical mirror of radius R is proportional to $\exp(-ik\rho^2/R)$. Therefore, the phase profile of the beam after reflection from the concave mirror is

$$\begin{aligned} \Phi_{\text{refl}}(\rho, \phi, z) &= k\rho^2(A(z) - 1/R) + \Phi_{\text{inc}}(\phi, z) \\ &= k\rho^2(A(z')) + \Phi_{\text{inc}}(\phi, z). \end{aligned} \quad (4)$$

This gives rise to the imaging equation

$$A(z') = A(z) - \frac{1}{R}. \quad (5)$$

For Gaussian beams, Eq. (5) reads

$$\frac{1}{\mathcal{R}(z')} = \frac{1}{\mathcal{R}(z)} - \frac{2}{R}. \quad (6)$$

As a result, if the mirror has the same curvature as the beam ($R = \mathcal{R}(z)$), the wave fronts of both the incident and reflected waves overlap, namely $\mathcal{R}(z') = -\mathcal{R}(z)$. Note that $\mathcal{R}(z)$ is positive since the incident wave is diverging, whereas $\mathcal{R}(z')$ is negative because the reflected wave is converging. We thus obtain the phase profile required for the metasurface to reflect the wave back onto itself:

$$\Phi_{\text{mirror}} = \frac{-k\rho^2}{\mathcal{R}(z)}. \quad (7)$$

We will use Eq. (7) in the following to calculate the reflection phase of the different elements composing the Gaussian metareflector.

In addition, the relation can also be extended to design a metasurface able to focus the reshaped beam to an arbitrary position z' . To this aim, we write

$$\mathcal{R}(z') = az'[1 + (z_0/z')^2] = b\mathcal{R}(z), \quad (8)$$

where a and b are constants, and from Eq. (8) we derive the ratio a/b as a function of z and z' :

$$\frac{a}{b} = \frac{z[1 + (z_0/z)^2]}{z'[1 + (z_0/z')^2]}. \quad (9)$$

Equation (9) yields two pairs of values, ($a < 0, b < 0$) and ($a > 0, b > 0$), for any given values of z and z' . However, one of the pairs leads to a nonphysical configuration. For instance, $a = b = -1$ yields $z = z'$ and $R = \mathcal{R}(z)$; whereas $a = b = 1$ also corresponds to $z = z'$ but gives rise to a configuration with $R = \infty$. Substituting Eqs. (3) and (8) into Eq. (6), we obtain the required radius of curvature of the metasurface,

$$R = \frac{2b}{b-1} \mathcal{R}(z) = \frac{2a}{b-1} z'[1 + (z_0/z')^2]. \quad (10)$$

The phase profile of the metasurface required to focus the reflected beam at an arbitrary position z' thus becomes

$$\Phi_{\text{mirror}} = \frac{(1-b)k\rho^2}{2b\mathcal{R}(z)} = \frac{(1-b)k\rho^2}{2az'[1 + (z_0/z')^2]}. \quad (11)$$

2.2. Building block optimization

Using the equations developed in the previous section, it is possible to design a Gaussian metareflector. The basic elements of the metasurface are identical dielectric nanofins of length L , width w , and height t [Fig. 1(d)] arranged in a lattice with unit cell size P and different orientations θ [Fig. 1(c)].

Thanks to the birefringent response of the dielectric nanofins with asymmetric cross-section [37], for appropriate values of their dimensions, a 2π phase coverage can be obtained by changing their angle of rotation θ between 0 and π . In this approach, known as geometrical phase or Berry-Pancharatnam (BP) phase metamaterials [38, 39], maximum polarization conversion efficiency is obtained when the nanofins function as half-wave plates, converting either left-handed or right-handed circularly polarized incident light to its orthogonal polarization state while inducing a phase shift of $\Phi = 2\theta$ ($\Phi = -2\theta$).

During the optimization of the building block, we maximize the polarization conversion efficiency in reflection, i.e., the cross-polarization reflection coefficient, S_{31} . We also require high and uniform amplitude in the entire $[0, 2\pi]$ phase range. To this aim, we perform numerical simulations of the building block using the finite-element method (COMSOL Multiphysics) with periodic boundary conditions in the x and y directions and circularly polarized incident light. We first compute the spectrum of S_{31} for a fixed value of θ and different values of the dimensions of the nanofins and the building block size. Thereafter, we span θ between 0 and π for optimized values of the other parameters to confirm that S_{31} has a uniform amplitude and complete 2π phase coverage.

2.3. Whole mirror

Finally, the whole mirror is designed by creating an array of nanofins with the optimized parameters found in the previous step on a two-dimensional lattice and rotating each nanofin in accordance with the phase map obtained before.

On the one hand, the phase shift Φ required for each nanofin in the lattice is computed from Eq. (7). On the other hand, the relationship between the angle of rotation θ and the phase shift Φ is obtained from the phase coverage simulations of the building block for different values of θ between 0 and π . The phase shift is related to the angle of the nanofins and a linear relationship with slope close to 1/2 between θ and Φ is often but not always obtained. In cases where the relationship between θ and Φ is not linear, which occurs because the near-field interaction

between neighboring nanofins changes with the orientation of the nanofins, the required values of θ can be obtained by interpolation from the data obtained from the phase coverage simulations.

As an example, a top view of a Gaussian metareflector is shown in Fig. 1(c). All the nanofins are identical and their angle of rotation is proportional to the inverse of the square of their distance from the center. This mirror is optimized for a wavelength of $\lambda = 700$ nm, has a focal length $f = 35$ μm , and a radius of 8.2 μm . Metareflectors with shorter focal length are possible; however, when the metasurface is closer to the focal point, the curvature of the phase fronts gets larger, which means that the required phase for reflection is changing faster over the surface of the metasurface. In order to accurately discretize the phase profile with the unit cells, a shorter focal length will ultimately require smaller unit cells, eventually leading to a limit imposed by fabrication.

The whole mirror is finally simulated with the finite-element method (COMSOL Multiphysics) for circularly polarized incident light. The simulation domain of the fully dielectric mirror is terminated with perfectly matched layers on the top and the bottom sides and a scattering boundary condition on the cylindrical side. The simulation domain of the metareflector with the metallic substrate is terminated with a perfectly matched layer on the top side, a perfect electric conductor on the bottom side, and a scattering boundary condition on the cylindrical side. Such a hybrid mirror does not require a perfectly matched layer on the bottom side due to the small value of the skin depth of the metallic substrate (smaller than 20 nm). The length of the simulation domain is limited by the available random-access memory and is shorter than the distance f between the beam waist of the Gaussian beam and the mirror. In order to calculate the focal point of the reflected beam, the scattered beam is propagated with a two-step method [40], wherein the Huygens-Fresnel (HF) principle [41] for beam propagation from spherical point scatterers in a source plane is used to propagate the field using Fresnel diffraction integrals. The HF method is limited by the requirement that the destination plane must be located in the far-field. The two-step method addresses this limitation by two subsequent propagation steps back and forth from a far-field dummy plane; hence, providing an approach for field propagation between a source and destination plane separated by an arbitrary distance. To compute the results we started from the electric field distributions obtained from the finite-element calculations (see Fig. 9 in the Appendix as an example) and then used the two-step method to propagate the fields to planes around the focal point of the reflected beam.

3. Results

3.1. Unit cell optimization

There are several possible material combinations that could be used to realize a reflective metasurface. Plasmonic, all-dielectric, and hybrid nanostructures have been extensively used for lenses and each materials system may be optimal for a particular wavelength range. Due to their smaller optical losses, we focus here on two materials systems, both composed of dielectric nanofins. In the first case, we design mirrors optimized for a free-space wavelength of $\lambda = 1064$ nm, a typical laser source in the near infrared of interest for optical tweezers. For this purpose, we use nanofins made of TiO_2 (data from Ref. [42]), a transparent material with a relatively large refractive index, placed on top of an Al mirror to minimize transmission of light [see the schematic in Fig. 2(a)]. In the second case, we design a fully dielectric metasurface for operation at shorter wavelengths. Here, we instead used Si nanofins (data from Ref. [43]) on top of a Si substrate (data from Ref. [44]) separated by a transparent dielectric spacer [see schematic in Fig. 2(d)].

The cross-polarized reflection spectrum S_{31} for the hybrid structure with TiO_2 nanofins on a metal substrate is shown in Fig. 2(b). With this structure, high efficiencies (80%-95%) can be obtained at wavelengths over 1000 nm for optimized values of the geometrical parameters. We found that, for the size here chosen (width $w = 80$ nm and length $L = 350$ nm), TiO_2 nanofins

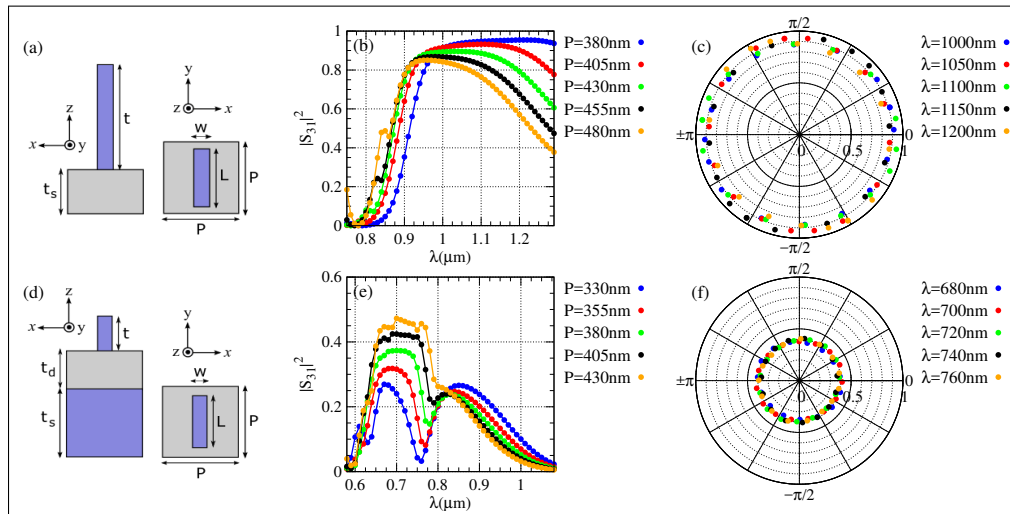


Fig. 2. Optimized hybrid and purely dielectric metasurfaces for reflection of focused beams: (a) Schematic of the hybrid structure with TiO₂ nanofins on an Al mirror. (b) Spectra of the cross-polarized reflectance $|S_{31}|^2$ for different sizes of the unit cell P . (c) Phase coverage of the hybrid structure for $P = 380$ nm at selected wavelengths. (d) Schematic of the fully dielectric metasurface with Si nanofins on top of a Si substrate separated by a SiO₂ spacer. (e) Spectra of the cross-polarized reflectance $|S_{31}|^2$ for different unit cell sizes P . (f) Phase coverage of the dielectric metasurface with Si nanofins for the same parameters as in (e) for $P = 400$ nm at selected wavelengths.

with a thickness of ≈ 700 nm allow the system to work as a half-wave plate in reflection. Similar results have also been obtained for Si nanofins on top of an Al mirror (see Appendix, Fig. 5). In this case, the optimized structures are thinner due to the higher refractive index of Si, but at the same time the cross-polarized reflection is diminished to 80% [see Fig. 5(a)] due to larger index mismatch between air and Si, leading to larger reflection in the co-polarized beam.

For both the Si and the TiO₂ nanofins, the hybrid dielectric-metal structures present a complete and almost uniform phase coverage [see the polar plots in Fig. 2(c) and Fig. 5 in the Appendix]: there is an almost linear relationship between the phase shift of reflection and the angle of rotation of the nanofins. This can be understood by noticing that these nanofins do not support any internal geometrical resonance (Mie type mode) at $\lambda > 1000$ nm; the reflection phase is due only to the birefringent propagation of the two orthogonal circularly polarized modes through the nanofin structure.

A very different situation is encountered for the fully dielectric structure, consisting of Si nanofins on a Si substrate [see schematic in Fig. 2(d)]. In this case, the spectral response exhibits a plateau of constant amplitude at around 700 nm [see Fig. 2(e) and Fig. 6]. The isolated nanofins ($t = 200$ nm, $w = 80$ nm, $L = 300$ nm) have an almost constant reflection amplitude (see Fig. 8 of the Appendix for the spectra of the isolated nanofins), which is the result of spectrally overlapping electric-dipole and magnetic-dipole resonances [45, 46]. The resulting spectrum is due to the far-field interference of light reflected from the nanofins and from the Si substrate. Changes in both spacing [300 nm in the plot of Fig. 2(d)] and period between the nanofins influence the interference conditions and the overall reflection. Despite being resonant, the nanostructure shows uniform phase coverage also in this case [see Fig. 2(f) and Fig. 7 in the Appendix] in the wavelength region where the reflection $|S_{31}|^2$ is spectrally flat.

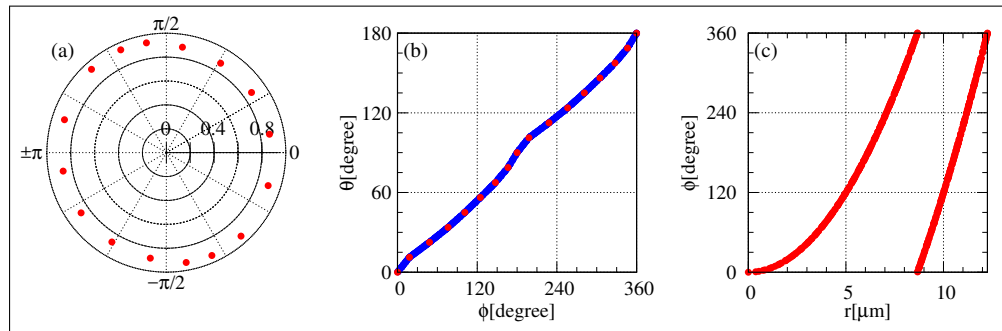


Fig. 3. Reflection phase response of the nanofins: (a) Phase coverage of the hybrid dielectric-metal structure with TiO_2 nanofins for $\lambda = 1064$ nm, $P = 380$ nm, and values of the other parameters as in Fig. 2(b). (b) Relation between the nanofin angle of rotation and the desired reflection phase used to determine the rotation of every individual fin to obtain the reflection phase distribution in (c). Red points correspond to the data from (a) and the blue line to the interpolation of this data. (c) Phase shift distribution required to build a metareflector for a Gaussian mirror of radius $12.57 \mu\text{m}$ and $\text{NA} = 0.24$ for a wavelength of $\lambda = 1064$ nm and focal length of $f = 50\lambda$ as a function of the distance to the center of the mirror discretized with the unit cell size $P = 380$ nm in the x and y directions.

3.2. Phase relation between the different nanofins

As discussed in Sec. 3.1, the results are qualitatively very similar for all the structures, but the reflection efficiency is different for each of the discussed configurations. Due to the larger cross-polarized reflection efficiency, we focus for the remainder of this article on the hybrid structure with TiO_2 nanofins on the Al mirror (see Figs. 10 and 11 in the Appendix for the results for other configurations). To design a full Gaussian metareflector, it is important to correlate the phase of each nanofin to its rotation angle with respect to the surface normal. To do so, we first verified full and almost homogeneous phase coverage of the cross-polarized reflected signal as a function of the nanofin angle at the wavelength of operation $\lambda = 1064$ nm [Fig. 3(a)]. Then we interpolated the polar plot to provide a 1-to-1 correspondence between the nanofin rotation and the phase of the reflected signal [Fig. 3(b)]. We observe once again that the relationship is not perfectly linear because of the changing near-field interactions with different orientations of the nanofins. To design the profile of the full Gaussian metareflector, we finally assumed a Gaussian beam that is strongly focused but for which the paraxial approximation [Eq. (4)] is still valid and we choose the Rayleigh distance equal to $1.02 \mu\text{m}$. Figure 3(c) shows the phase relation for a Gaussian metasurface as a function of the radial distance from the mirror center according to Eq. (7). To extract the exact positions and orientations of the nanofins, we finally fixed the optimal distance between the nanofins as $P = 380$ nm, discretized the phase of each nanofin at multiple values of P in a square lattice, and converted the corresponding phase to a physical rotation angle for each nanofin. The result of such a procedure was already shown in Fig. 1(c). It is interesting to point out that the difference in phase between consecutive elements grows quadratically with the distance; for a too large angle the phase gradient will be too large and the phase distribution will not be well discretized with the unit cell size used. This ultimately implies a trade-off between the diameter of the mirror, the distance to the focal point, and the numerical aperture.

3.3. Whole mirror

In Fig. 4, the quality of the reflected beam is analyzed for the TiO_2 -on-Al metasurface (see Figs. 10 and 11 in the Appendix for the purely dielectric metasurface and for the hybrid metasurface with

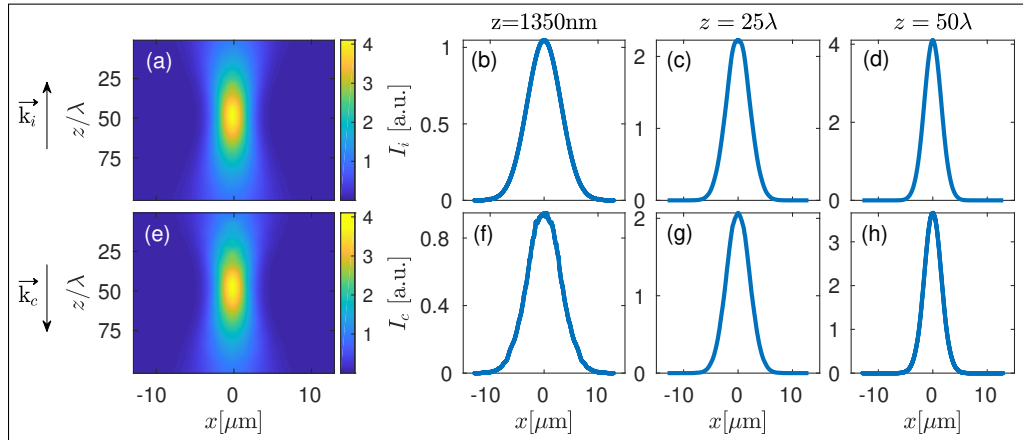


Fig. 4. Simulation results of the hybrid Gaussian metasurface built with TiO_2 nanofins on top of an Al substrate, optimized at the trapping wavelength $\lambda = 1064$ nm with unit cell size $P = 380$ nm and the values of the other parameters as in Fig. 2(b). This mirror has a radius of $12.57 \mu\text{m}$, and a focal length $f = 50\lambda = 53 \mu\text{m}$. Top: Intensity distribution of the incident Gaussian field (I_i) as a function of the distance z scaled with λ (a), at $z = 1350$ nm (b), at $z = 25\lambda$ (c) and at the focal distance $z = f = 50\lambda$ (d). Bottom: Intensity distribution of the cross-polarized reflected field (I_c) as a function of the distance z scaled with λ (e), at $z = 1350$ nm (f), at $z = 25\lambda$ (g), and at the focal distance $z = f = 50\lambda$ (h).

Si nanofins). The plot shows the beam profile obtained from propagating the optical field using the two-step method. The entire reflective metasurface has radius $R_m = 12.57 \mu\text{m}$, so that it covers 99.9% of the total power in the incident beam, and a focal length of $f = 50\lambda$.

First, it is important to note that the cross-polarized reflected beam [Fig. 4(e)] is nearly identical to the incident Gaussian beam [Fig. 4(a)] and that the back-focusing takes place at the expected focal distance $f = 50\lambda$. Plots of the intensity distribution at different distances show that the beam radius is the same for the incident beam [Fig. 4(b)–4(d)] and the cross-polarized reflected beam [Fig. 4(f)–4(h)]. In particular, the beam waist of the Gaussian beam is $w_0 = (3.21 \pm 0.02) \mu\text{m}$ for both the incoming [Fig. 4(d)] and the reflected beam [Fig. 4(h)].

The intensity of the reflected beam is also consistent with the reflection coefficient calculated above for the nanofins. For example, in Fig. 4(g), the peak intensity of the reflected beam is about 90% of the peak intensity of the incident beam. From our simulations, we estimate that about 9% of the intensity is lost by dissipation in the materials and about 1% is lost by conversion to co-polarized reflection (which is a divergent beam not focused back to the focal point of the incident beam).

In addition, the quality of the reflection can be assessed from the reflection phase at a plane between the metasurface and the focal point of the beam, as in Fig. 12 in the Appendix. We see again an excellent agreement between the reflection phase created by our metareflector and the ideal phase of a reflected beam perfectly overlapping with the incident beam.

4. Conclusion

We have proposed a design method for metasurfaces that can manipulate nonplanar wavefronts. As an example, we have designed a Gaussian reflective metasurface, i.e., the metasurface equivalent of a concave spherical mirror. We demonstrated that such metasurfaces can produce a reflected cross-polarized beam that perfectly overlaps with the incident field. Our optimized designs have power efficiencies over 90%, obtained by using TiO_2 nanofins as metasurface building block

placed on an Al back mirror. Such a metasurface building block ensures minimal losses, together with a homogeneous and complete phase coverage. We envision several applications for reflective metasurfaces like the ones presented in this article. For example, they could be used to realize ultracompact reflective mirrors and confocal microcavities or could be used as mirrors in optical tweezers and other nanophotonic devices.

A. Appendix

A.1. Optimization of the unit cell

A.1.1. Optimization of dielectric nanofins on an Al mirror

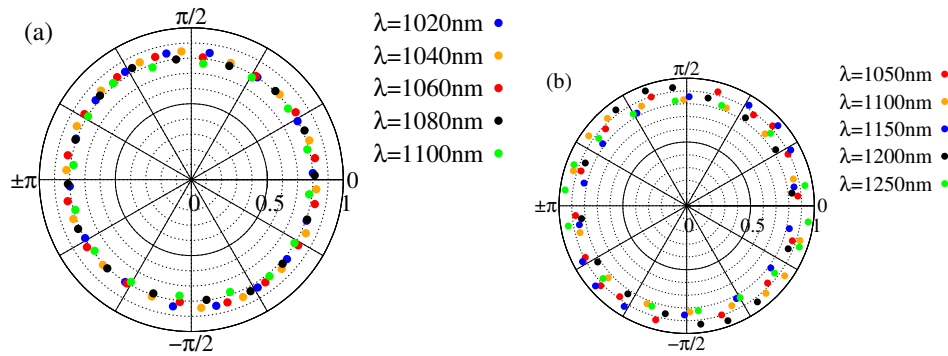


Fig. 5. Phase coverage of hybrid structures made of Si (a) and TiO_2 (b) nanofins of width $w = 80$ nm, heights $t = 200$ nm (a) and $t = 800$ nm (b), and length $L = 350$ nm patterned on an Al substrate of thickness $t_s = 300$ nm with unit cell size $P = 380$ nm.

A.1.2. Optimization of the dielectric structure

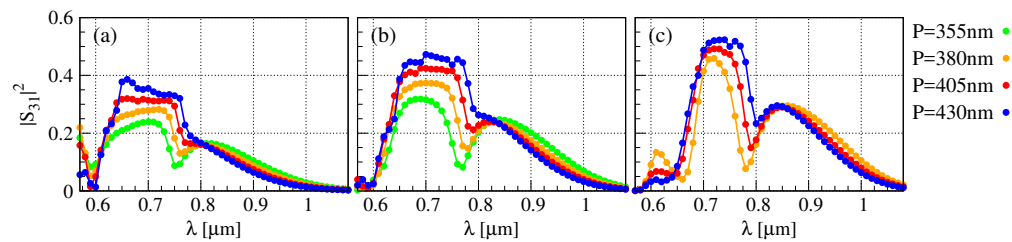


Fig. 6. Spectra of the cross-polarized reflectance $|S_{31}|^2$ of the dielectric structure made of Si nanofins of width $w = 80$ nm, height $t = 200$ nm, lengths $L = 250$ nm (a), $L = 300$ nm (b) and $L = 350$ nm (c) and angle of rotation $\theta = 0$ on top of Si substrate of thickness $t_s = 700$ nm with a SiO_2 spacer of thickness $t_d = 300$ nm. $|S_{31}|^2$ increases by increasing L or the unit cell size P .

A.2. Simulations of fully dielectric reflector

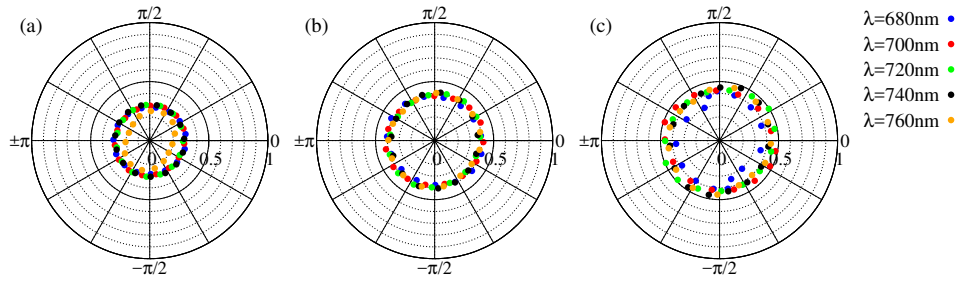


Fig. 7. Phase coverage of the dielectric structure for the same parameters as in Fig. 6(a) [Fig. 7(a)], Fig. 6(b) [Fig. 7(b)], and Fig. 6(c) [Fig. 7(c)] but keeping the unit cell size fixed to $P = 400$ nm and for wavelength values within the plateau of constant reflectance $|S_{31}|^2$. The radial coordinate is $|S_{31}|^2$ and the angular coordinate is the phase angle of S_{31} .

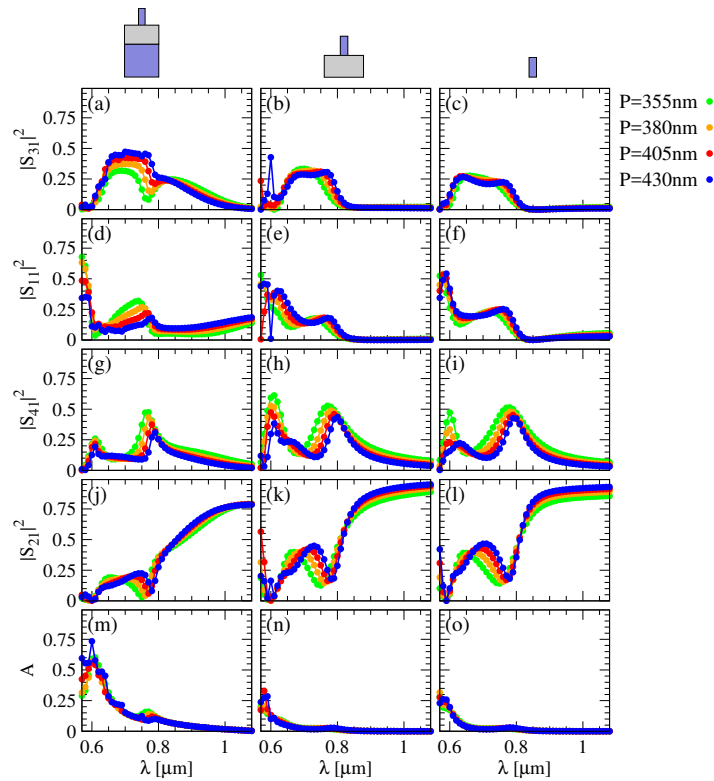


Fig. 8. Spectra of the [(a)-(c)] cross- and [(d)-(f)] co-polarized reflected and [(g)-(i)] cross- and [(j)-(l)] co-polarized transmitted intensities, and [(m)-(o)] absorption loss for [(a), (d), (g), (j), (m)] the dielectric structure, [(b), (e), (h), (k), (n)] the dielectric structure without the Si substrate and [(c), (f), (i), (l), (o)] the standalone Si nanofin in air, for the parameter values as in Fig. 6. The outliers at the smallest wavelengths are due to a too coarse mesh—a finer mesh is not possible with the available computer resources. For wavelengths above 650 nm, the accuracy is better than 1%.

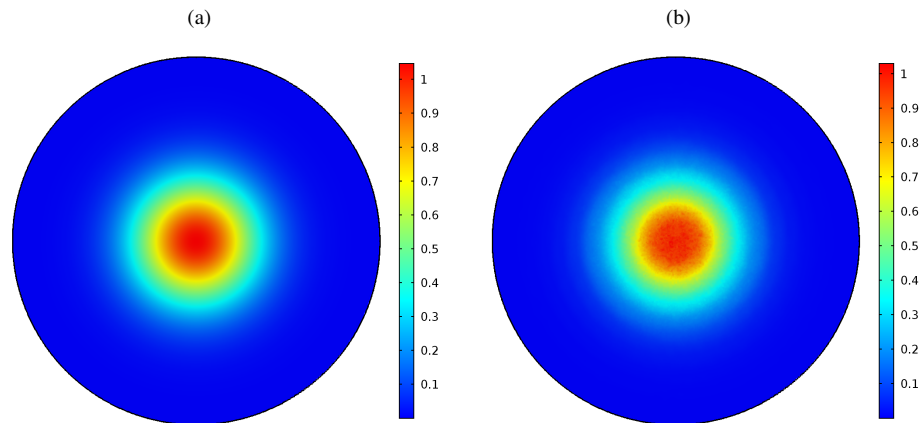


Fig. 9. Intensity of the (a) incident and (b) cross-polarized reflected field at the initial plane $z = 1350$ nm used in the 2-step method for the hybrid structure with TiO_2 nanofins on Al with parameter values as in Fig. 4 of the main text.

A.3. Whole mirror

A.3.1. Field propagation with the two-step method

A.3.2. Dielectric mirror

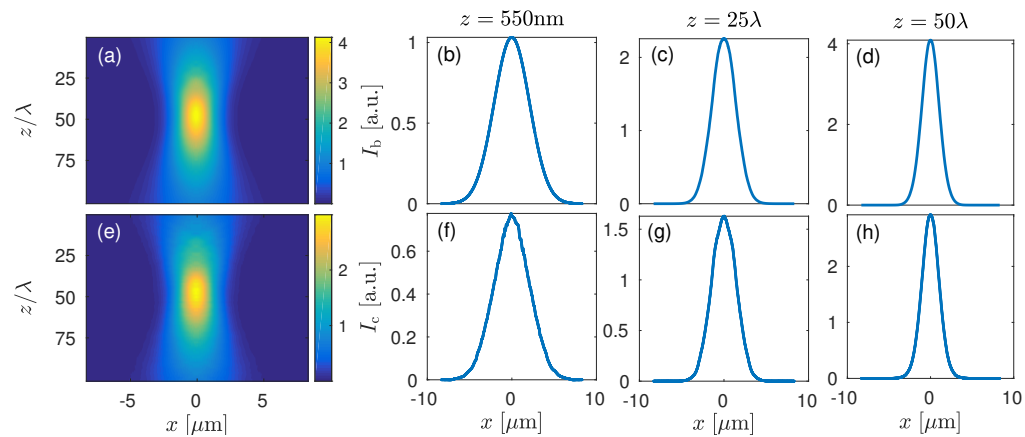


Fig. 10. Simulation results of the dielectric mirror built with Si nanofins on top of a poly-Si substrate with a SiO_2 spacer, optimized at the typical trapping wavelength $\lambda = 700$ nm with the values of the other parameters as in Fig. 7(b). This mirror has a radius of $8.2 \mu\text{m}$ and a focal length $f = 35 \mu\text{m}$, giving a numerical aperture $\text{NA} = 0.23$. Top: Intensity distribution of the incident field (I_b) as a function of the distance z scaled with λ (a), at $z = 550$ nm (b), at $z = 25\lambda$ (c) and at the focal distance $z = f = 50\lambda$ (d). Bottom: Intensity distribution of the cross-polarized reflected field (I_c) as a function of the distance z scaled with λ (e), at $z = 550$ nm (f), at $z = 25\lambda$ (g) and at the focal distance $z = f = 50\lambda$ (h).

A.3.3. Hybrid mirror with Si nanofins on Al

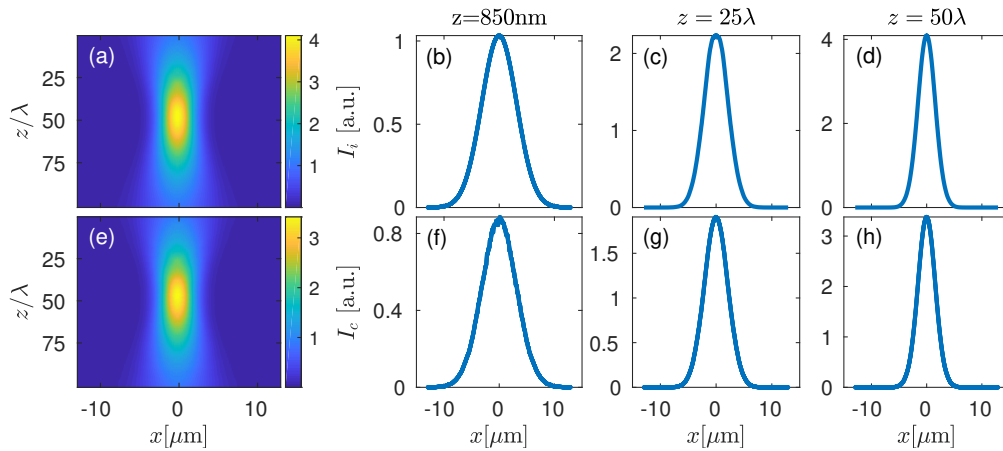


Fig. 11. Simulation results of the hybrid Gaussian mirror built with Si nanofins on top of an Al substrate, optimized at the typical trapping wavelength $\lambda = 1064$ nm with the values of the other parameters as in Fig. 5(a). This mirror has a radius of $12.57 \mu\text{m}$ and a focal length $f = 50\lambda$, giving a numerical aperture $\text{NA} = 0.24$. Top: Intensity distribution of the incident Gaussian field (I_i) as a function of the distance z scaled with λ (a), at $z = 850$ nm (b), at $z = 25\lambda$ (c) and at the focal distance $z = f = 50\lambda$ (d). Bottom: Intensity distribution of the cross-polarized reflected field (I_c) as a function of the distance z scaled with λ (e), at $z = 850$ nm (f), at $z = 25\lambda$ (g) and at the focal distance $z = f = 50\lambda$ (h).

A.3.4. Reflected phase profile

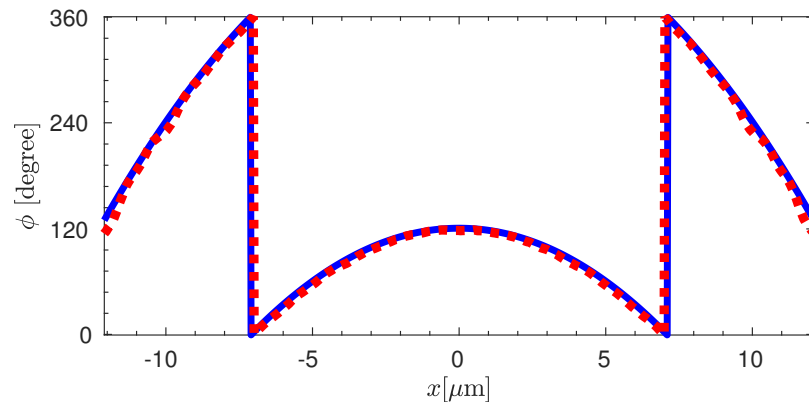


Fig. 12. Phase of the ideal Gaussian field (blue line) and cross-polarized reflected field (red dotted line) at the plane $z = 1350$ nm for the hybrid structure with TiO_2 nanofins on Al with parameter values as in Fig. 4 of the main text.

Acknowledgments

The authors would like to thank N. Odebo Länk for useful discussions. Work at Chalmers was supported financially by the Knut and Alice Wallenberg Foundation and the Chalmers' Excellence

Initiative Nano and was supported by access to high-performance computing equipment provided by the Swedish National Infrastructure for Computing (SNIC).

Disclosures

The authors declare that there are no conflicts of interest related to this article.

References

1. N. Yu, P. Genevet, M. A. Kats, F. Aieta, J.-P. Tetienne, F. Capasso, and Z. Gaburro, "Light propagation with phase discontinuities: Generalized laws of reflection and refraction," *Science* **334**, 333–337 (2011).
2. A. V. Kildishev, A. Boltasseva, and V. M. Shalaev, "Planar photonics with metasurfaces," *Science* **339**, 1232009 (2013).
3. N. Yu and F. Capasso, "Flat optics with designer metasurfaces," *Nat. Mater.* **13**, 139–150 (2014).
4. P. Genevet, F. Capasso, F. Aieta, M. Khorasaninejad, and R. Devlin, "Recent advances in planar optics: from plasmonic to dielectric metasurfaces," *Optica* **4**, 139 (2017).
5. F. Falcone, T. Lopetegi, M. A. Laso, J. D. Baena, J. Bonache, M. Beruete, R. Marques, F. Martín, and M. Sorolla, "Babinet principle applied to the design of metasurfaces and metamaterials," *Phys. Rev. Lett.* **93**, 197401 (2004).
6. H.-H. Hsiao, C. H. Chu, and D. P. Tsai, "Fundamentals and applications of metasurfaces," *Small Methods* **1**, 1600064 (2017).
7. D. Berry, R. Malech, and W. Kennedy, "The reflectarray antenna," *IEEE Trans. Antennas Propag.* **11**, 645–651 (1963).
8. D. M. Pozar and T. A. Metzler, "Analysis of a reflectarray antenna using microstrip patches of variable size," *Electron. Lett.* **29**, 657–658 (1993).
9. J. A. Encinar, "Design of two-layer printed reflectarrays using patches of variable size," *IEEE Trans. Antennas Propag.* **49**, 1403–1410 (2001).
10. P. Padilla, A. Muñoz-Acevedo, M. Sierra-Castañer, and M. Sierra-Pérez, "Electronically reconfigurable transmitarray at Ku band for microwave applications," *IEEE Trans. Antennas Propag.* **58**, 2571–2579 (2010).
11. C. G. Ryan, M. R. Chaharmir, J. Shaker, J. R. Bray, Y. M. Antar, and A. Ittipiboon, "A wideband transmitarray using dual-resonant double square rings," *IEEE Trans. Antennas Propag.* **58**, 1486–1493 (2010).
12. A. Alù, "Mantle cloak: Invisibility induced by a surface," *Phys. Rev. B* **80**, 245115 (2009).
13. J. C. Soric, P. Y. Chen, A. Kerkhoff, D. Rainwater, K. Melin, and A. Alù, "Demonstration of an ultralow profile cloak for scattering suppression of a finite-length rod in free space," *New J. Phys.* **15**, 033037 (2013).
14. N. M. Estakhri and A. Alù, "Ultra-thin unidirectional carpet cloak and wavefront reconstruction with graded metasurfaces," *IEEE Antennas Wirel. Propag. Lett.* **13**, 1775–1778 (2014).
15. X. Ni, Z. J. Wong, M. Mrejen, Y. Wang, and X. Zhang, "An ultrathin invisibility skin cloak for visible light," *Science* **349**, 1310–1314 (2015).
16. K. Aydin, V. E. Ferry, R. M. Briggs, and H. A. Atwater, "Broadband polarization-independent resonant light absorption using ultrathin plasmonic super absorbers," *Nat. Commun.* **2**, 517 (2011).
17. P. Spinelli, M. A. Verschuuren, and A. Polman, "Broadband omnidirectional antireflection coating based on subwavelength surface Mie resonators," *Nat. Commun.* **3**, 692 (2012).
18. N. Engheta, "Thin absorbing screens using metamaterial surfaces," in *IEEE Antennas and Propagation Society International Symposium*, vol. 2 (2002), pp. 392–395.
19. P. Y. Chen and A. Alù, "Subwavelength imaging using phase-conjugating nonlinear nanoantenna arrays," *Nano Lett.* **11**, 5514–5518 (2011).
20. T. Roy, E. T. F. Rogers, and N. I. Zheludev, "Sub-wavelength focusing meta-lens," *Opt. Express* **21**, 7577–7582 (2013).
21. F. Aieta, P. Genevet, M. A. Kats, N. Yu, R. Blanchard, Z. Gaburro, and F. Capasso, "Aberration-free ultrathin flat lenses and axicons at telecom wavelengths based on plasmonic metasurfaces," *Nano Lett.* **12**, 4932–4936 (2012).
22. M. Kang, T. Feng, H.-T. Wang, and J. Li, "Wave front engineering from an array of thin aperture antennas," *Opt. Express* **20**, 15882 (2012).
23. C. Pfeiffer and A. Grbic, "Cascaded metasurfaces for complete phase and polarization control," *Appl. Phys. Lett.* **102**, 231116 (2013).
24. M. A. Al-Joumayly and N. Behdad, "Wideband planar microwave lenses using sub-wavelength spatial phase shifters," *IEEE Trans. Antennas Propag.* **59**, 4542–4552 (2011).
25. V. Ginis, P. Tassin, T. Koschny, and C. M. Soukoulis, "Broadband metasurfaces enabling arbitrarily large delay-bandwidth products," *Appl. Phys. Lett.* **108**, 031601 (2016).
26. Y. Zhao, M. A. Belkin, and A. Alù, "Twisted optical metamaterials for planarized ultrathin broadband circular polarizers," *Nat. Commun.* **3**, 870 (2012).
27. L. Huang, X. Chen, B. Bai, Q. Tan, G. Jin, T. Zentgraf, and S. Zhang, "Helicity dependent directional surface plasmon polariton excitation using a metasurface with interfacial phase discontinuity," *Light. Sci. Appl.* **2**, 1–7 (2013).
28. N. Yu, F. Aieta, P. Genevet, M. A. Kats, Z. Gaburro, and F. Capasso, "A broadband, background-free quarter-wave plate based on plasmonic metasurfaces," *Nano Lett.* **12**, 6328–6333 (2012).

29. G. T. Oumbé Tékam, V. Ginis, J. Danckaert, and P. Tassin, "Designing an efficient rectifying cut-wire metasurface for electromagnetic energy harvesting," *Appl. Phys. Lett.* **110**, 083901 (2012).
30. O. Tsilipakos, A. C. Tasolamprou, T. Koschny, M. Kafesaki, E. N. Economou, and C. M. Soukoulis, "Pairing Toroidal and Magnetic Dipole Resonances in Elliptic Dielectric Rod Metasurfaces for Reconfigurable Wavefront Manipulation in Reflection," *Adv. Opt. Mater.* **6**, 1800633 (2012).
31. M. Khorasaninejad and F. Capasso, "Metalenses: Versatile multifunctional photonic components," *Science* **358**, eaam8100 (2017).
32. M. Khorasaninejad, W. T. Chen, R. C. Devlin, J. Oh, A. Y. Zhu, and F. Capasso, "Metalenses at visible wavelengths: Diffraction-limited focusing and subwavelength resolution imaging," *Science* **352**, 1190–1194 (2016).
33. Q. Fan, P. Huo, D. Wang, Y. Liang, F. Yan, and T. Xu, "Visible light focusing flat lenses based on hybrid dielectric-metal metasurface reflector-arrays," *Sci. Rep.* **7**, 1–9 (2017).
34. A. E. Minovich and A. V. Zayats, "Geometric-phase metasurfaces based on anisotropic reflection: Generalized design rules," *ACS Photon.* **5**, 1755–1761 (2018).
35. S. Wang, P. Chieh Wu, V.-C. Su, Y.-C. Lai, M.-K. Chen, H. Yu Kuo, B. Han Chen, Y. Han Chen, T.-T. Huang, J.-H. Wang, R.-M. Lin, C.-H. Kuan, T. Li, Z. Wang, S. Zhu, and D. P. Tsai, "A broadband achromatic metalens in the visible," *Nat. Nanotech.* **13**, 227–232 (2018).
36. A. Yariv and P. Yeh, *Optical Waves in Crystals* (Wiley, 1984).
37. D. C. Flanders, "Submicrometer periodicity gratings as artificial anisotropic dielectrics," *Appl. Phys. Lett.* **42**, 492–494 (1983).
38. S. Pancharatnam, "Generalized theory of interference and its applications," *Proc. Natl. Acad. Sci. India A* **44**, 247–262 (1956).
39. M. V. Berry, "The adiabatic phase and Pancharatnam's phase for polarized light," *J. Mod. Opt.* **34**, 1401–1407 (1987).
40. C. Rydberg and J. Bengtsson, "Efficient numerical representation of the optical field for the propagation of partially coherent radiation with a specified spatial and temporal coherence function," *J. Opt. Soc. Am. A* **23**, 1616–1625 (2006).
41. B. E. Saleh and M. C. Teich, *Fundamentals of Photonics* (Wiley, 1991).
42. J. R. DeVore, "Refractive indices of rutile and sphalerite," *J. Opt. Soc. Am.* **41**, 416–419 (1951).
43. M. A. Green, "Self-consistent optical parameters of intrinsic silicon at 300 K including temperature coefficients," *Sol. Energy Mater. Sol. Cells* **92**, 1305–1310 (2008).
44. R. Verre, N. O. Länk, D. Andrén, H. Šipová, and M. Käll, "Large-Scale Fabrication of Shaped High Index Dielectric Nanoparticles on a Substrate and in Solution," *Adv. Opt. Mater.* **6**, 1701253 (2018).
45. P. Moitra, B. A. Slovick, W. Li, I. I. Kravchenko, D. P. Briggs, S. Krishnamurthy, and J. Valentine, "Large-Scale All-Dielectric Metamaterial Perfect Reflectors," *ACS Photon.* **2**, 692–698 (2015).
46. O. Tsilipakos, T. Koschny, and C. M. Soukoulis, "Antimatched Electromagnetic Metasurfaces for Broadband Arbitrary Phase Manipulation in Reflection," *ACS Photon.* **5**, 1101–1107 (2018).